Progress In Electromagnetics Research C, Vol. 150, 69-80, 2024

(Received 9 July 2024, Accepted 5 November 2024, Scheduled 12 November 2024)

A Current Sensorless Interval Torque Ripple Suppression Method for Permanent Magnet assisted-Switched Reluctance Motor

Chengyi Gong, Junxin Xu*, Renquan Xiao, Chaozhi Huang, Xiaobo Liu, and Yong Xiao

School of Electrical Engineering and Automation, Jiangxi University of Science and Technology, Ganzhou 341000, Jiangxi, China

ABSTRACT: The conventional DITC strategy for switched reluctance motor relies on current for control, while the use of current sensors increases the complexity of the system, and the torque ripple in the two-phase exchange region of the conventional DITC strategy is too large. To solve the above problems, a current sensorless interval torque control (CSITC) method is proposed. Initially, the equivalence between torque and acceleration control is established, replacing the torque loop with an acceleration loop. This forms a dual closed-loop system with the speed control loop, enhancing system stability. Subsequently, the variation of the output torque capacity of phase winding of the motor in each conduction region is analyzed, and combined with the inductive characteristics of the motor windings, the two-phase exchange region is divided into two subregions. Different acceleration hysteresis loop control strategies are adopted for the phase windings in each region, so as to realize the stable output of the motor torque. Finally, a three-phase 6/20 permanent magnet assisted-switched reluctance motor (PMa-SRM) is used for simulation and physical verification. The results show that the method can still achieve the steady state of the motor when only the position sensor is used and effectively reduces the torque ripple in the exchange region.

1. INTRODUCTION

PMa-SRM has been widely recognized by scholars for its advantages of high power density, simple structure, and good speed regulation compared to the conventional SRM [1–5]. PMa-SRM increases the motor power density to improve the torque output capability by embedding permanent magnets in the stator slot to improve the motor performance. PMa-SRM increases the motor power density by embedding permanent magnets in the stator slot to increase the torque output capability and improve the motor performance, as shown in Figure 1.

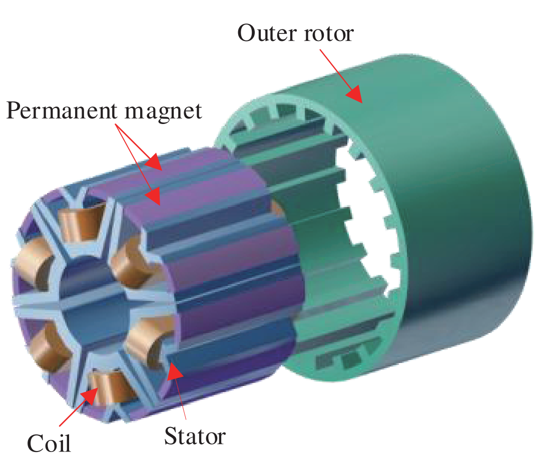

FIGURE 1. PMa-SRM structure diagram.

However, the unique double-convex pole structure of PMa-SRM and the unique way of pulse power supply lead to large torque ripple and noise during operation, which limits its promotion and application in the industrial field. Therefore, how to effectively reduce the torque ripple of PMa-SRM is the focus of research.

To address this challenge, scholars mainly research from two aspects: first, optimizing the motor structure [6–8], but this is not conducive to the motors that have been produced or applied. The second is to optimize the control strategy, which not only is easy to implement, but also has a lower cost. Currently, the main control strategies for suppressing PMa-SRM torque ripple is pulse width modulation (PWM) [9], torque sharing function control (TSF) [10], and direct instantaneous torque control (DITC) [11]. The above control strategies are effective in suppressing the torque ripple, but all of them require current as a feedback quantity to control the motor torque, which requires high accuracy of the motor model parameters.

Usually, the current sensor of SRM is installed at the end of the phase winding to facilitate the collection of current signals. The use of current sensors has the following drawbacks: (I) It increases the cost and size of the system; (II) The installation requires additional wiring, which brings about circuit interference and reduces the system reliability; (III) It is subject to environmental constraints, and it may be inaccurate or fail in harsh environments [12, 13]. In order to reduce the number of current sensors to improve system reliability and save costs, many scholars have conducted related research. Ref. [14] proposed

* Corresponding author: Junxin Xu (xujx9997@163.com).

doi:10.2528/PIERC24070901

to use only one current sensor to reconstruct the phase currents of a PWM inverter in a DC-link, which effectively reduces the voltage harmonics and minimizes the audible noise. Ref. [15] reconfigured both the power converter and current sensor to reduce the number of current sensors used to one. For the two operating phases in the exchange region, the method obtains current values by switching the measurements. Ref. [16] proposed a six-phase current reconfiguration scheme for a dual traction inverter using a single DC-link current sensor, which reduces the number of current sensors used and lowers the cost, but produces unwanted interference to the PWM signals. Ref. [17] proposed a current reconstruction technique that used only one current sensor to measure the current in a three-phase inverter. Ref. [18] proposed two novel power converter reconfiguration techniques to reconfigure the phase currents, which reduced the size of the system and improved the performance. Many scholars have also sampled the winding currents by designing observers. Refs. [19–21] used Luenberger state observers and sliding mode observers to estimate the phase currents in order to reduce the use of current sensors; however, these methods rely on accurate mathematical modeling of the motor.

Therefore, in order to take into account the cost as well as the reliability of the system, this paper proposes a current sensorless interval torque control method. Firstly, the equivalence between torque control and acceleration control is verified, and the torque loop in the conventional torque control is replaced by an acceleration loop, which constitutes a double closed-loop system with the speed loop, and the feasibility is analyzed. Secondly, to solve the problem of large torque ripple in the two-phase exchange region of PMa-SRM, we analyze the inductance characteristics of the motor, divide the two-phase exchange region into two subregions, and adopt different acceleration hysteresis loop control strategies for each region, so as to control the conduction and shutting off the switching tubes and to realize the stabilized output of the motor torque. Finally, Matlab/Simulink simulation software is used to conduct simulation experiments and build an experimental platform for testing to verify the effectiveness of the proposed control strategy.

2. FEASIBILITY OF CURRENT SENSORLESS

2.1. Direct Instantaneous Torque Control

A three-phase 6/20 PMa-SRM is taken as the object of study, and the main circuit adopts a three-phase asymmetric half-bridge converter (AHBC), as shown in Figure 2. The AHBC can make full use of the power supply voltage and change the number of winding phases at will. Each phase of the AHBC can be operated independently in different modes, and it is commonly used to drive SRM [22].

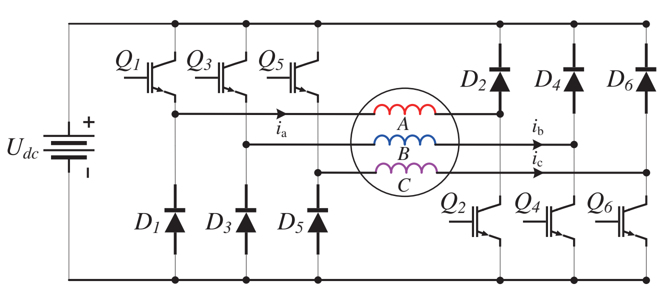

FIGURE 2. Three-phase asymmetrical half-bridge power converter.

The DITC strategy consists primarily of three modules: PID module, instantaneous torque estimation module, and hysteresis loop controller. The instantaneous torque estimation module calculates the motor's actual torque in real-time based on current and position signals obtained from corresponding sensors. It then compares this estimated torque with the reference torque output from the PID module. The disparity between these two values is fed into the hysteresis loop controller. This controller operates according to a predefined hysteresis control strategy, determining the power converter's conduction signals. These signals effectively regulate the motor's operation, as illustrated in Figure 3.

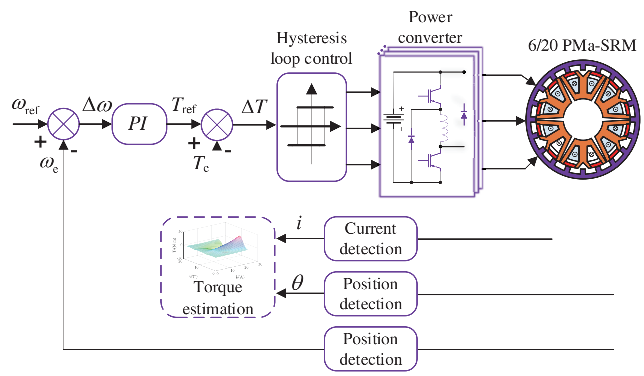

FIGURE 3. DITC block diagram.

As shown in Figure 4, the region from the phase B turn-on angle θ_{on}^{B} to the phase A fully aligned position θ_{e}^{B} is the two-phase exchange region (TpE), and the region from the A-phase fully aligned position θ_{e}^{B} to the phase C turn-on angle θ_{on}^{C} is the single phase conduction region (SpC).

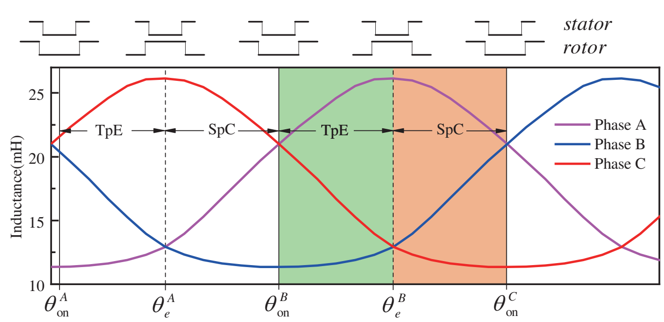

FIGURE 4. Schematic diagram of conventional DITC partitioning.

The switching mode of each phase of the PMa-SRM is jointly determined by the torque error and the rotor position in the DITC strategy. The torque error is defined as:

$$\Delta T = T_{\text{ref}} - T_{\text{e}} \tag{1}$$

where ΔT, T_{ref}, and T_e are the torque error, reference torque, and instantaneous torque, respectively.

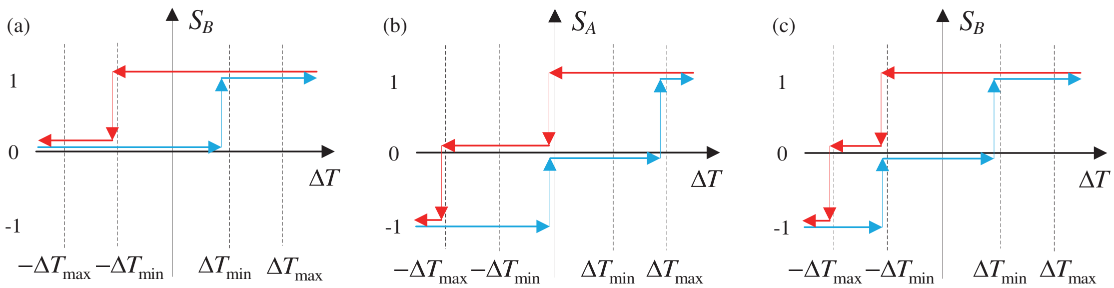

FIGURE 5. Conventional DITC hysteresis loop strategy. (a) Excitation phase in TpE region. (b) Demagnetization phase in TpE region. (c) SpC region.

The hysteresis loop strategies of the conventional DITC in the excitation and demagnetization phases in the TpE and SpC are shown in Figures 5(a), (b), and (c), respectively.

2.2. Equivalence of Acceleration Control and Torque Control

In any of the control methods for switched reluctance motors, the rotor position and speed need to be accurately obtained. Typically, the rotor position can be acquired directly from the position sensor, and the velocity as well as the acceleration can be obtained by taking the first and second order derivatives with respect to time, while the third and higher orders are not physically meaningful and therefore not solved for. When the system relies on a single position sensor, only the acceleration can provide information for feedback in addition to the speed feedback.

According to the laws of mechanics, the mechanical equation of motion of the motor is given by:

$$T_{\mathrm{e}}(t) = J\frac{\mathrm{d}\omega(t)}{\mathrm{d}t} + D\omega(t) + T_{\mathrm{L}} \tag{2}$$

where $T_e(t)$ is the electromagnetic torque; T_L is the load torque; J is the moment of inertia; D is the friction coefficient.

As the motor speed converges to a given speed, the difference between the two is a very small value δ, which can be expressed as:

$$\left|\ \omega_{\mathrm{ref}}(t) - \omega(t)\ \right| < \delta \tag{3}$$

where $\delta = \omega_{\mathrm{ref}}(t)$, then Equation (2) can be expressed as:

$$T_{\mathrm{e}}(t) = J\frac{\mathrm{d}\omega(t)}{\mathrm{d}t} + D\omega_{\mathrm{ref}}(t) + D\delta + T_{\mathrm{L}} \tag{4}$$

Eq. (5) can be obtained by neglecting $D\delta$ in Eq. (4):

$$T_{\mathrm{e}}(t) \approx J\frac{\mathrm{d}\omega(t)}{\mathrm{d}t} + D\omega_{\mathrm{ref}}(t) + T_{\mathrm{L}} = J\frac{\mathrm{d}\omega(t)}{\mathrm{d}t} + C_1 \tag{5}$$

where C_1 is the sum of $D\omega_{\mathrm{ref}}(t)$ and T_L and is a constant. Its value changes only when the reference speed and load torque change.

From Equation (5), it can be obtained that there is an approximate linear relationship between acceleration and electromagnetic torque. In order to verify the conclusion, the simulation model is built in Matlab/Simulink, and the electromagnetic torque and acceleration waveforms are simulated and compared. The results are shown in Figure 6. Under the working condition of 1000 rpm rotational speed and 10 N·m load, the amplitude of electromagnetic torque and acceleration approximately shows a linear relationship. From the above, it can be seen that in order to suppress the torque ripple of the motor, only the acceleration ripple of the motor needs to be effectively suppressed.

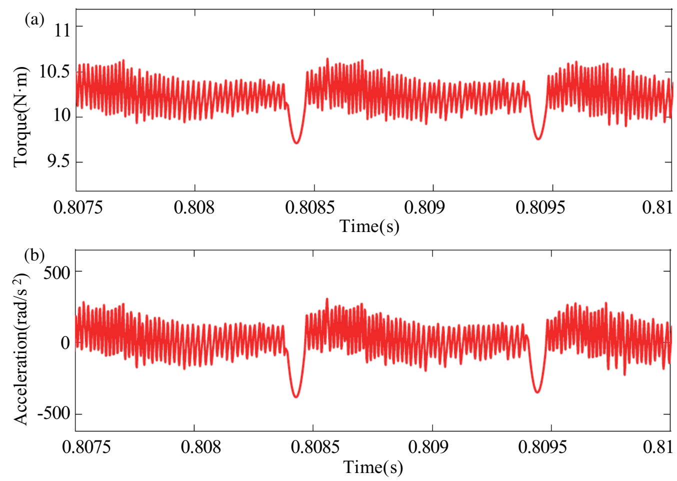

FIGURE 6. Schematic diagram of torque and acceleration at speed 1000 rpm. (a) Torque waveform schematic. (b) Acceleration waveform schematic.

2.3. Stability of Closed-Loop Control of Acceleration

Since the current sensor is removed from the motor system, there is no current feedback signal. In the case where only the position sensor is used, a velocity, acceleration double closed loop is taken to control the motor. The feasibility of this control method is analyzed below. Since acceleration is a real-time variable, it is approximated:

$$\frac{\mathrm{d}\omega(t)}{\mathrm{d}t} = \left[\frac{\mathrm{d}\omega(t)}{\mathrm{d}t}\right]_{\mathrm{ref}} \tag{6}$$

where $\omega(t)$ is the rotational speed; t is the time; $d\omega(t)/dt$ is the real time acceleration; $[d\omega(t)/dt]_{ref}$ is the reference acceleration. Since the reference acceleration is output via the PI controller, there is:

$$\begin{aligned}\frac{\mathrm{d}\omega(t)}{\mathrm{d}t} &= \left(\frac{\mathrm{d}\omega(t)}{\mathrm{d}t}\right)_{\mathrm{ref}} \\ &= K_{\mathrm{P}}\left\{[\omega_{\mathrm{ref}}(t)-\omega(t)]+\frac{1}{T_{\mathrm{I}}}\int_{0}^{t}[\omega_{\mathrm{ref}}(\lambda)-\omega(\lambda)]\,\mathrm{d}\lambda\right\}\end{aligned} \tag{7}$$

where K_p is the proportionality constant of the PI regulator; $\omega_{ref}(t)$ is the given rotational speed; T_I is the integration constant.

From Equation (7), the transfer function of the system is Laplace transformed from time domain to frequency domain:

$$\frac{\omega(s)}{\omega_{\mathrm{ref}}(s)} = \frac{K_{\mathrm{P}}s + \frac{K_{\mathrm{P}}}{T_{\mathrm{I}}}}{s^2 + K_{\mathrm{P}}s + \frac{K_{\mathrm{P}}}{T_{\mathrm{I}}}} \tag{8}$$

where s is the complex frequency. The poles of this transfer function can be obtained from Equation (8):

$$x_{1,2} = \frac{-K_p \pm \sqrt{K_p^2 - 4\frac{K_p}{T_I}}}{2} \tag{9}$$

From the stability criterion in the complex frequency domain, the closed-loop system is stable when the poles of the transfer function of the closed-loop system are all in the left half plane of the S-plane. As shown in Equation (4), since K_p and T_I in the power integrity (PI) regulator are positive, the poles $x_{1,2}$ are in the left half plane of the S-plane. Therefore, this closed-loop system is stable.

3. INTERVAL ACCELERATION HYSTERESIS CONTROL STRATEGY

Based on the equivalence analysis of torque control and acceleration control, acceleration hysteresis loop method is used in this paper to track the instantaneous acceleration to stabilize the motor electromagnetic torque output. The conventional DITC strategy uses only a single hysteresis loop control strategy in TpE, and the demagnetized phase may still be excited in the later part of TpE, generating large torque ripples. To solve this problem, this paper proposes a partitioned interval current sensorless torque ripple suppression strategy. By analyzing the changes of the output torque capacity of the phase windings of the motor in each conduction region, combined with the inductive characteristics of the motor windings, a rotor cycle is divided into three regions of TpE I, TpE II, and SpC, combined with the equivalence of acceleration and torque control. The corresponding acceleration hysteresis loop control strategy is designed for different regions, and the control block diagram is shown in Figure 7.

3.1. PMa-SRM Partitioning Based on Rate Change of Inductance

As depicted in Figure 8, the inductance characteristics of the PMa-SRM exhibit saturation effects that vary with different

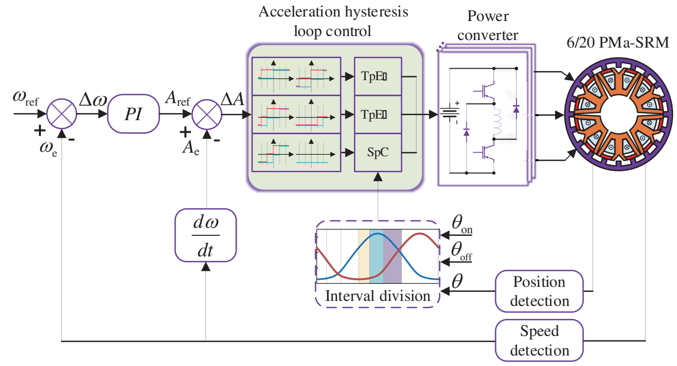

FIGURE 7. CSITC block diagram.

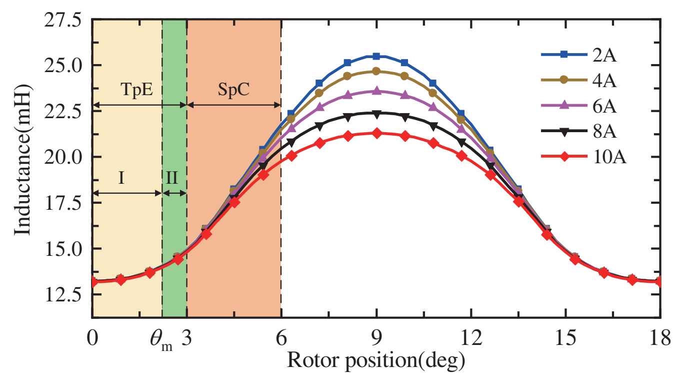

FIGURE 8. PMa-SRM inductance curve clusters.

current magnitudes, displaying a declining trend as current increases. However, upon examining the cluster of inductance curves, it becomes evident that the rate of change in inductance is nearly negligible from the fully non-aligned position to θ_m. Beyond θ_m, there is a pronounced increase in the rate of inductance change. Here, θ_m denotes the inductance boundary point, a fixed value.

From the above, it can be seen that the two-phase exchange region is divided into TpE I and TpE II by the inductance boundary point θ_m, as shown in Figure 9. To analyze the phase A demagnetization phase and phase B excitation phase, the starting point of TpE I is the opening angle θ_{on}^{B}, and the inductance and inductance change rate of the phase B in this area are small, and the electromagnetic torque generated is much smaller than the torque required for the motor operation, so the torque required for the motor operation in this area is almost all provided by phase A, and at this time, three-phase synthesized torque ripple is also mainly generated by phase A.

When the rotor continues to move and enters TpE II, the inductance of phase B rises significantly. The starting point of TpE II is θ_{m}^{B}. At this time, the inductance change rate of phase A decreases rapidly. The ability to provide torque is weakened, and vice versa, the ability to provide torque of phase B is strengthened. The position of the demagnetized phase where the stator and rotor are fully aligned is defined as θ_{e}, which is a fixed value. When the rotor enters the SpC region ($\theta_{\mathrm{e}}^{B} \sim \theta_{\mathrm{on}}^{C}$), the inductance change rate of phase A is less than zero, generating a negative torque, and at this time, phase A should always

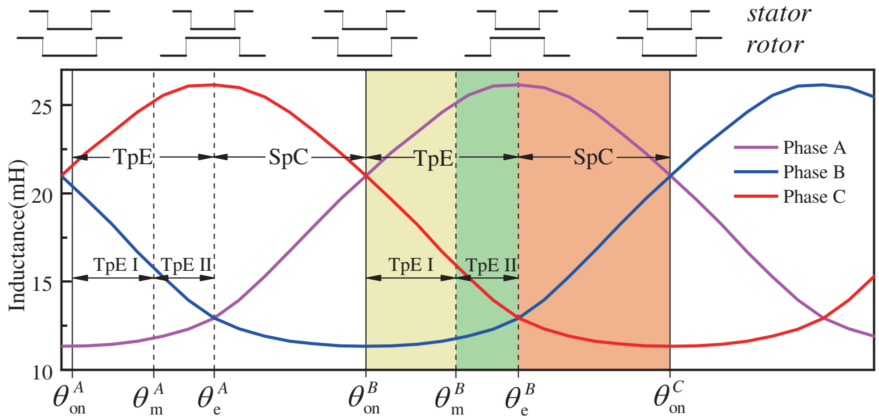

FIGURE 9. PMa-SRM partition based on inductance change rate.

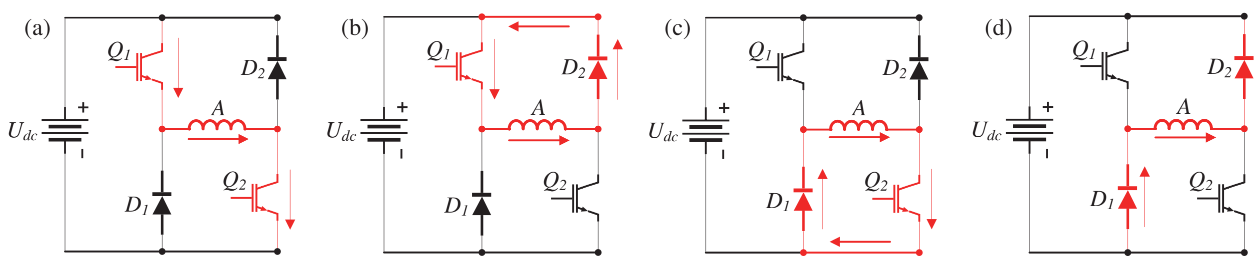

FIGURE 10. Operating states of the power converter. (a) Excitation state. (b) Continuation state I. (c) Continuing current state II. (d) Demagnetization state.

be turned off, while the inductance change rate of the phase B has reached its maximum value, and the output torque of the motor in the region is supplied solely by phase B.

3.2. Principle of Acceleration Hysteresis Control

Currently, the SRM control model generally involves an electrical flow rate and is therefore not applicable under conditions without a current sensor. Due to the equivalence of torque control and acceleration control, there exists an upper acceleration hysteresis loop limit $\Delta A_{\max}$ and a lower limit $\Delta A_{\min}$. In this paper, $\Delta A_{\max}$ is 15 rad/s^2, and $\Delta A_{\min}$ is 7.5 rad/s^2. The acceleration error is set to ΔA, and there is:

$$\begin{aligned}\Delta A &= \mathrm{d}\omega_{\mathrm{ref}}(\mathrm{t})/\mathrm{dt} - \mathrm{d}\omega_{\mathrm{e}}(\mathrm{t})/\mathrm{dt} \\ &= A_{\mathrm{ref}} - A_{\mathrm{e}}\end{aligned} \tag{10}$$

where A_{ref} is the reference acceleration, output by the PI controller; A_e is the instantaneous acceleration.

3.2.1. Relationship between Power Changer State and Acceleration

There are four operating states of AHBC when the PMa-SRM operates, which are illustrated in phase A as an example, as shown in Figure 10. As shown in Figure 10(a), when Q_1 and Q_2 conduct at the same time, the phase windings are excited, at which time the current increases resulting in a rise in torque. According to Equation (5), the torque and acceleration are approximately linearly related, so the acceleration also shows a rising trend. As shown in Figure 10(b), when Q_1 is on and Q_2 off, the phase winding voltage is zero, and in the continuation current state I, the acceleration decreases slowly. Similarly, when Q_2 conducts, and Q_1 turns off, the phase voltage is zero for the continuation state II, as shown in Figure 10(c). Finally, when both Q_1 and Q_2 are turned off, the phase winding is subjected to negative voltage for demagnetization, and the acceleration decreases rapidly, as shown in Figure 10(d).

3.2.2. Acceleration Hysteresis Loop Control

Taking phases A and B as an example, where B represents the excitation phase and A the demagnetization phase, in TpE I, immediately after the stator and rotor depart from the fully unaligned position, phase B exhibits a minor rate of inductance change, resulting in lower torque capacity. To swiftly enhance torque in phase B, a higher frequency of "1" states should be implemented. To avoid excessive current, if ΔA falls below $-\Delta A_{\max}$, the hysteresis loop switches to the "0" state for current continuity, ensuring a smooth decrease in A_e, as illustrated in Figure 11(a). Conversely, phase A experiences a substantial rate of inductance change during this phase, serving as the primary contributor to motor torque. Figure 11(b) illustrates the acceleration hysteresis loop strategy, which guarantees consistent output torque.

As the rotor enters TpE II, the stator and rotor of the demagnetized phase A approach full alignment, causing the rate of inductance change to gradually decrease towards zero. To minimize the negative torque resulting from residual current, the

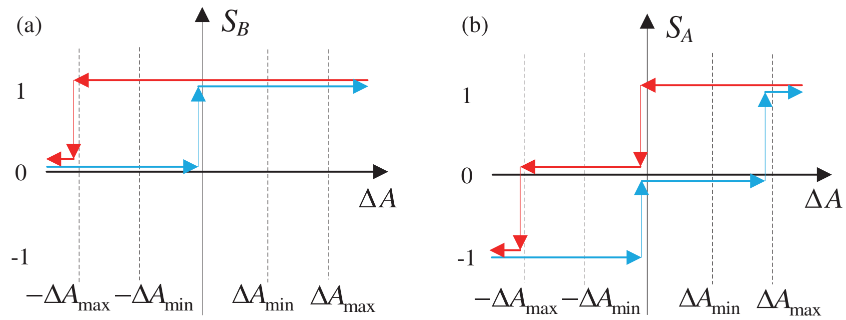

FIGURE 11. Hysteresis loop strategy for TpE I. (a) Excitation phase. (b) Demagnetization phase.

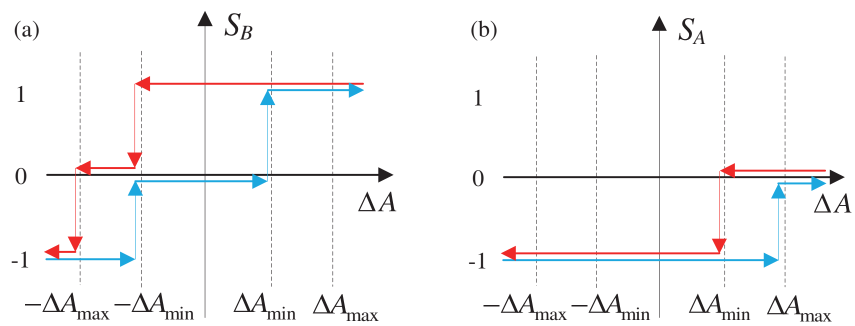

FIGURE 12. Hysteresis loop strategy for TpE II. (a) Excitation phase. (b) Demagnetization phase.

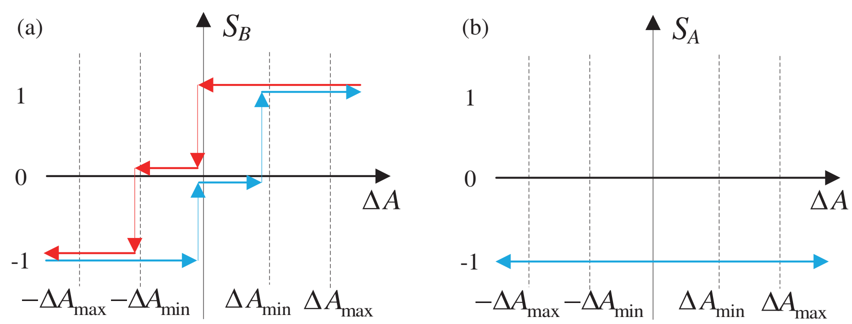

FIGURE 13. Hysteresis loop strategy in SpC. (a) Excitation phase. (b) Demagnetization phase.

demagnetized phase is configured with more "-1" state in this zone to rapidly reduce current. The hysteresis loop remains at "0" to resume current only when ΔA exceeds $\Delta A_{\max}$, ensuring a smooth decrease in A_e, as depicted in Figure 12(b). Conversely, during the rapid increase in A_e and torque capacity of excitation phase B in this phase, if ΔA progressively exceeds $\Delta A_{\min}$, the hysteresis loop shifts to "1" to boost A_e swiftly. Conversely, if ΔA gradually decreases below $-\Delta A_{\min}$, the hysteresis loop remains at "0" to smooth the decline in A_e. Should ΔA continue to decrease to $-\Delta A_{\max}$, the hysteresis state shifts to "-1" to prevent excessive winding current and mitigate torque ripple, as illustrated in Figure 12(a).

When the rotor enters SpC, the inductance change rate of demagnetized phase A becomes negative. Continuing to excite phase A under these conditions would generate significant negative torque, thereby reducing motor efficiency. To mitigate this, phase A remains consistently in the "-1" state throughout this phase, facilitating rapid current decay, as illustrated in Figure 13(b). Meanwhile, the inductance change rate of excitation phase B remains relatively constant. To maintain constant output torque, the hysteresis loop state transitions to "1" and "-1" only when ΔA exceeds $\Delta A_{\min}$ or is less than -$\Delta A_{\min}$, promoting swift winding excitation and demagnetization, as depicted in Figures 13(a) and 12(b).

4. SIMULATION VERIFICATION

To validate the viability of CSITC strategy, we utilized a three-phase 6/20 PMa-SRM as an experimental prototype and developed a corresponding control simulation model in the Matlab/Simulink environment. Detailed motor parameters are presented in Table 1.

The conventional DITC method and proposed control method are compared and analyzed under conditions of low speed and light load, as well as high speed and heavy load, respectively. To quantitatively assess the effectiveness of these

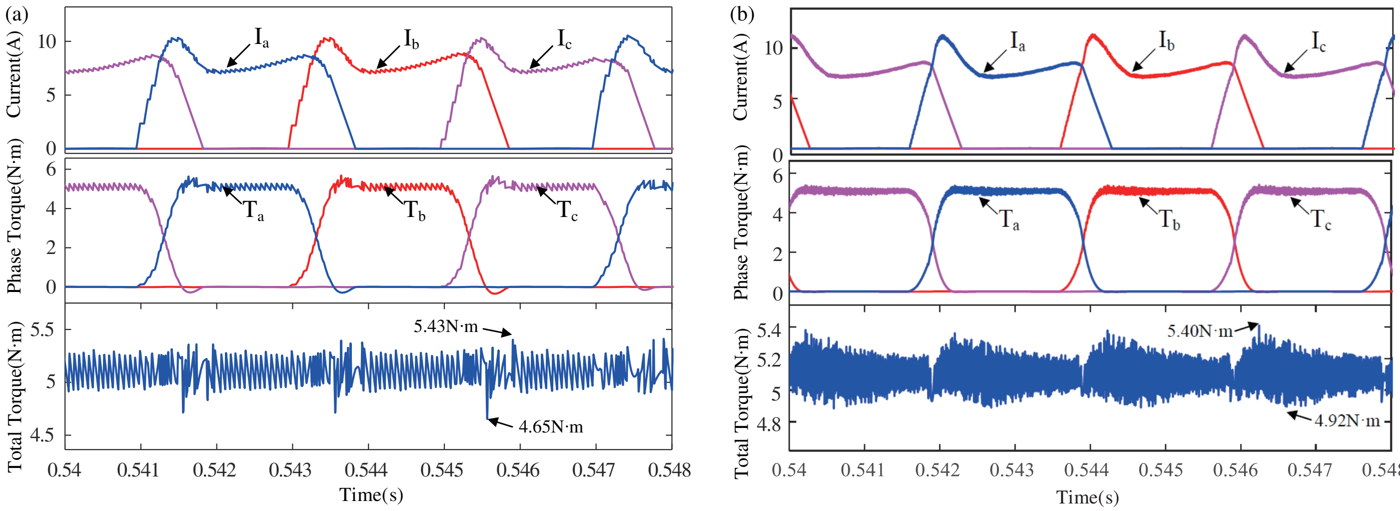

FIGURE 14. Simulation results under two control strategies (500 rpm, 5 N·m). (a) Conventional DITC control. (b) Proposed control strategy.

TABLE 1. PMa-SRM parameters.

Parameters	Values	Parameters	Values
Stator poles	6	Rotor tooth height/mm	6
Rotor poles	20	Stator tooth height/mm	6
Windings turns	55	Phase number	3
Stack length/mm	100	Rated voltage/V	540
Rotor diameter/mm	172	Rated current/A	30
Stator diameter/mm	142	Gap length/mm	0.6

methods in reducing motor torque ripple, we use the torque ripple coefficient K_T, defined as:

$$K_{\mathrm{T}} = \frac{T_{\max} - T_{\min}}{T_{\mathrm{avg}}} \times 100\% \tag{11}$$

where $T_{\max}$ and $T_{\min}$ are the maximum and minimum values of the threephase synthesized torque of the motor under steady state operation, respectively, and T_{avg} is the average value of the torque.

In the simulation experiment, the setting and completely unaligned position of the rotor (the coincidence position of the salient pole center of the stator and the center of the rotor groove) is 0°, and the turn-on and turn-off angles are 0° and 6°, respectively. At the speed of 500 rpm and under 5 N·m load, the waveforms of current, phase torque, and total torque for both control strategies are depicted in Figures 14(a) and (b). Under conditions of low speed and light load, the difference in torque ripple between the two control strategies is not significant. However, the motor torque exhibits greater stability under the proposed strategy, yielding torque ripple coefficient K_T of 15.6% and 9.6%, respectively. The conventional DITC strategy overlooks the nuances of excitation and demagnetization phases. At the transition between TpE and SpC phases, the demagnetization phase A enters a "-1" state, causing torque decrease rapidly. Consequently, the actual torque A_e exceeds the reference torque A_{ref}. The SpC hysteresis strategy sets phase B to "-1" to mitigate A_e, leading to a sharp decline in total torque and resulting in significant torque ripple in phase exchange region. In contrast, the method proposed in this paper confines the excitation phase B to "0" and "1" states in TpE I to swiftly enhance current. In TpE II, the excitation phase is governed by an accelerated internal hysteresis loop, switching to "-1" only when ΔA is less than $-\Delta A_{\max}$ for demagnetization purposes. In TpE II, the demagnetization phase employs multiple "-1" states to rapidly reduce current. The hysteresis loop shifts to "0" only when ΔA exceeds $\Delta A_{\max}$ to renew current, facilitating rapid current increase. This approach ensures that A_e decreases smoothly by maintaining the hysteresis loop state as "0" for current continuation when ΔA surpasses $\Delta A_{\max}$, effectively reducing negative torque and torque ripple.

As shown in Figures 15(a) and (b), when the load is increased to 10 N·m, K_T of the two control strategies are 16% and 6.5%, respectively. In comparison to the 5 N·m load, the proposed control strategy further minimizes torque ripple K_T. This enhancement is achieved because phase B is energized within the hysteresis loop set to "1" during TpE I, swiftly boosting instantaneous acceleration under heavy load conditions. During the initial half of TpE II, the rate of inductance change in phase B increases rapidly, managed by an internal hysteresis loop. Here, the hysteresis loop state shifts to "-1" for demagnetization only when ΔA is less than $-\Delta A_{\max}$, effectively reducing A_e and thereby lowering T_e. In the latter half of TpE II, the hysteresis loop of phase A switches to "0" to maintain current flow when total torque is inadequate, ensuring a smooth decrease in current. Concurrently, remaining moments are maintained at "-1" for demagnetization, minimizing negative torque as much as possible.

At 1000 rpm rotational speed and under a 5 N·m load, Figures 16(a) and (b) depict waveforms illustrating two distinct control strategies, with K_T values of 27% and 9.4%, respectively. These strategies demonstrate effective suppression of K_T in SpC. However, in TpE, conventional DITC prioritizes exciting the active phase to boost torque and demagnetizing the inactive phase to reduce it. To ensure timely tracking of

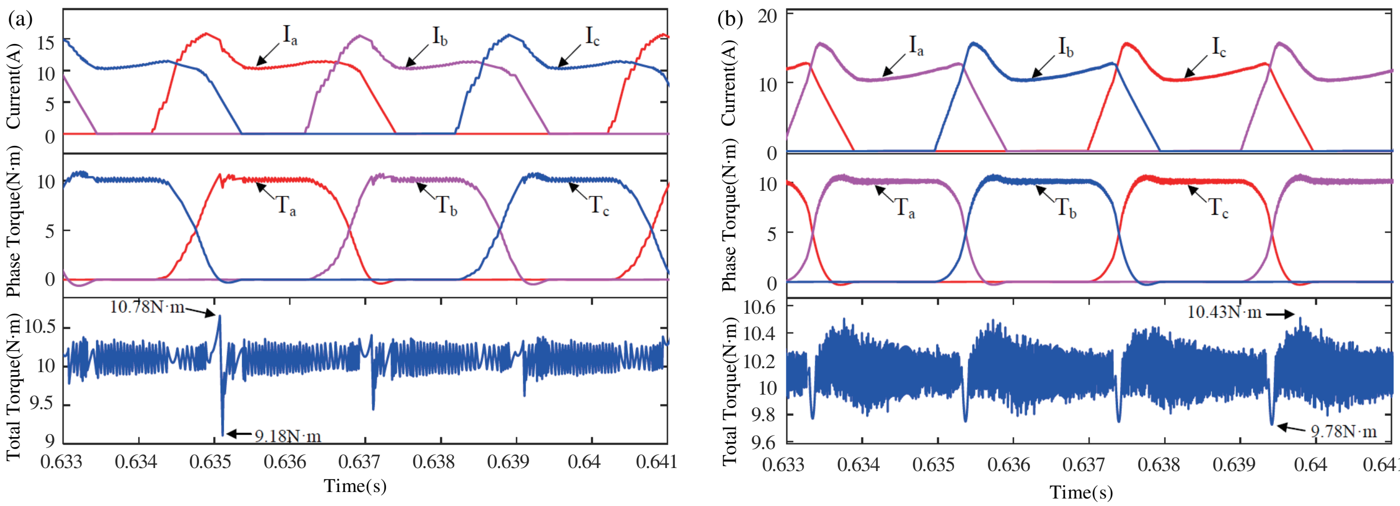

FIGURE 15. Simulation results under two control strategies (500 rpm, 10 N·m). (a) Conventional DITC control. (b) Proposed control strategy.

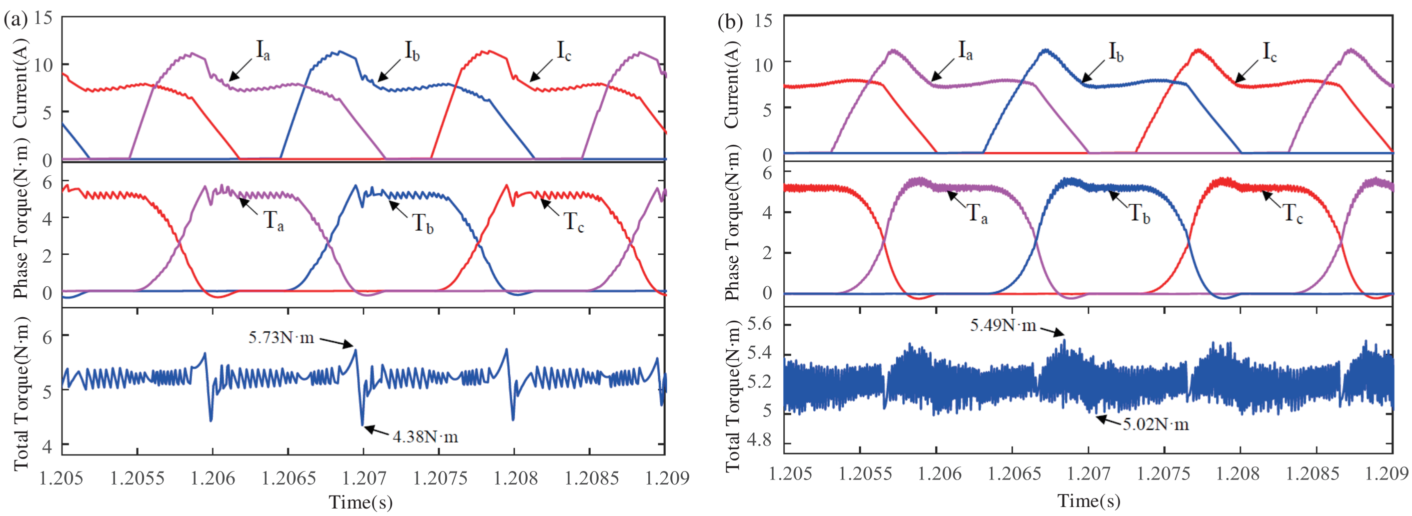

FIGURE 16. Simulation results under two control strategies (1000 rpm, 5 N·m). (a) Conventional DITC control. (b) Proposed control strategy.

the torque reference, phase B maintains a hysteresis loop state of "1" in the initial TpE phase for rapid current amplification, while phase A utilizes external hysteresis loop control for primary torque output. Later in TpE, rapid demagnetization of phase A decreases the total torque, resulting in significant torque ripple. In contrast, the proposed strategy leverages motor inductance and torque characteristics to regulate acceleration deviation using phases with superior torque output capability. Different acceleration hysteresis loop control strategies are employed in TpE I and TpE II, stabilizing and optimizing torque output.

Figures 17(a) and (b) illustrate the waveforms under two control strategies when the speed remains at 1000 rpm, and the load increases to 10 N·m. Figure 17(a) demonstrates that under the conventional DITC strategy, the motor fails to operate normally under high speed and heavy load conditions. In this scenario, the excitation phase B current in TpE has a short rise time, resulting in inadequate torque generation and an unbalanced three-phase synthesized torque. Subsequently, the rotor enters SpC, where the actual rotational speed ω_e still does not match the reference speed ω_{ref}. This discrepancy is input into the PI controller, causing a larger output reference acceleration A_{ref}. Despite this, the actual acceleration fails to track the reference, further amplifying the control error K_T. In contrast, the proposed control strategy demonstrates stable operation under these conditions. In TpE I, when ΔA exceeds 0, the excitation phase's hysteresis loop is set to "1" rapidly increasing winding current and augmenting A_e. If ΔA surpasses ΔA_{max}, the demagnetization phase's hysteresis loop is set to "1" to excite the winding, ensuring timely tracking of A_{ref}. This approach enables stable motor torque output, as depicted in Figure 17(b).

In order to see the superiority of the proposed control strategy more clearly, the simulation results of the above two control strategies are summarized in Table 2.

5. EXPERIMENTAL VERIFICATION

To further validate the proposed control strategy, experimentation was conducted using a three-phase 6/20 PMa-

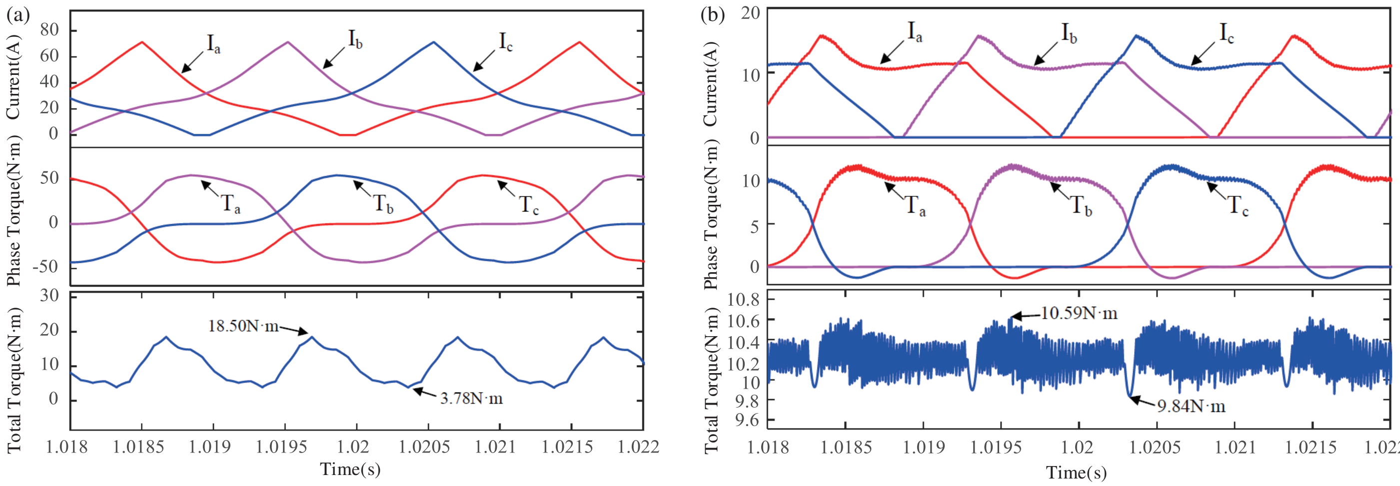

FIGURE 17. Simulation results under two control strategies (1000 rpm, 10 N·m). (a) Conventional DITC control. (b) Proposed control strategy.

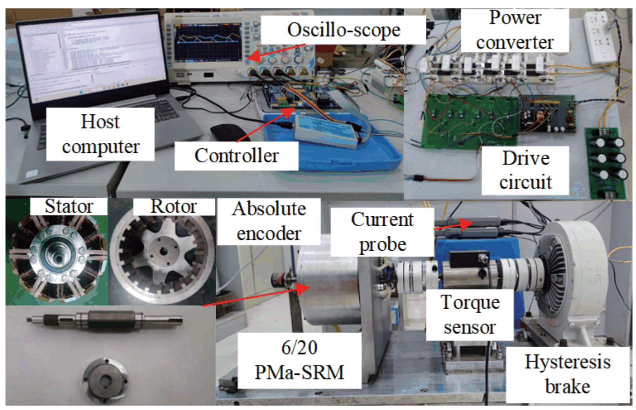

FIGURE 18. Experimental platform.

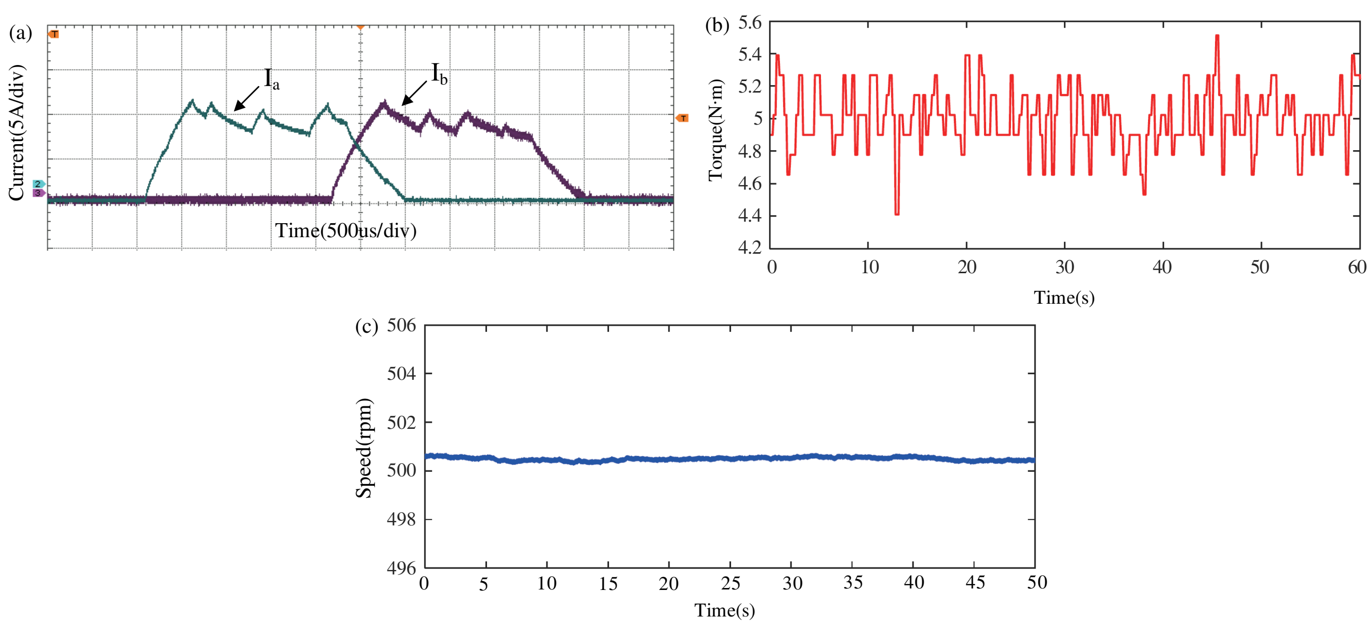

FIGURE 19. Current torque and speed waveforms under speed 500 rpm and load 5 N·m. (a) Current waveforms under conventional DITC. (b) Torque waveforms under conventional DITC. (c) Speed waveforms under conventional DITC.

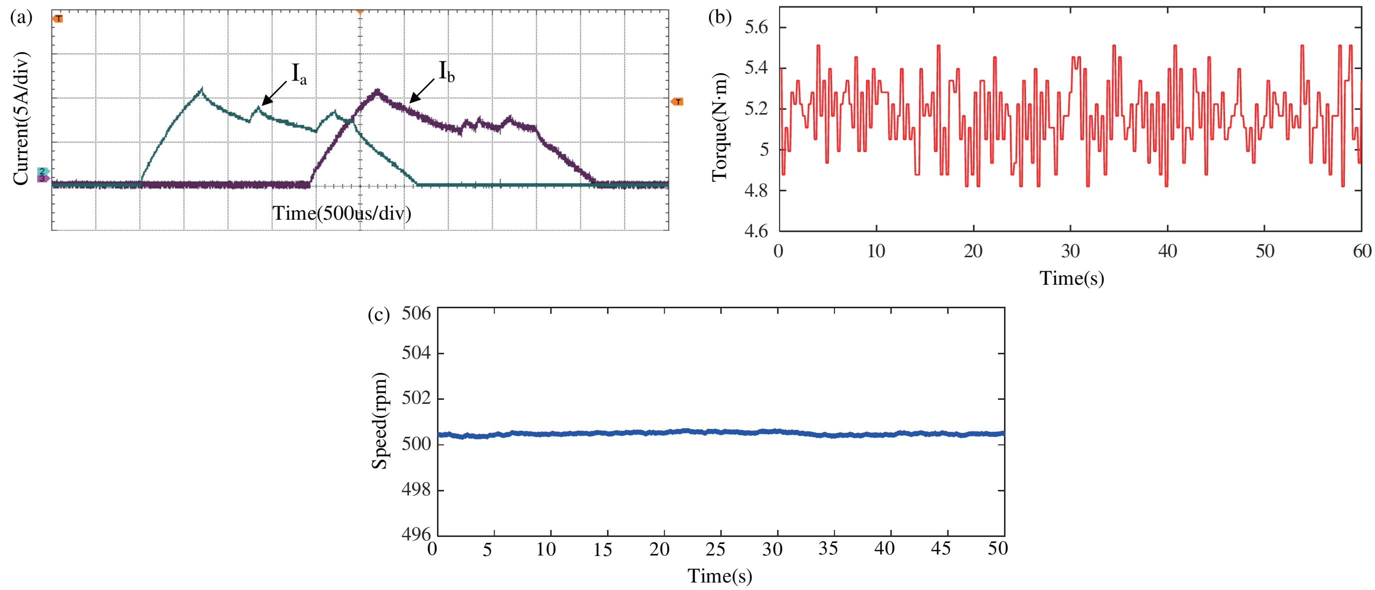

FIGURE 20. Current torque and speed waveforms under speed 500 rpm and load 5 N·m. (a) Current waveforms under the proposed strategy. (b) Torque waveforms under the proposed strategy. (c) Speed waveforms under the proposed strategy.

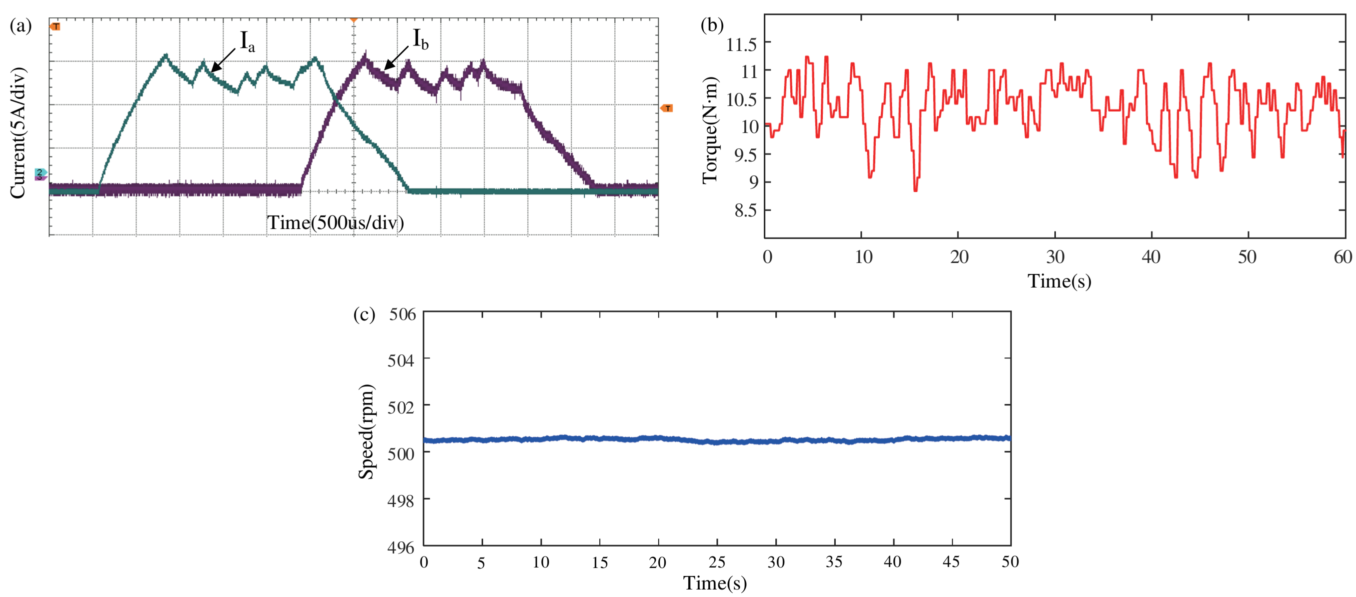

FIGURE 21. Current torque and speed waveforms under speed 500 rpm and load 10 N·m. (a) Current waveforms under conventional DITC. (b) Torque waveforms under conventional DITC. (c) Speed waveforms under conventional DITC.

SRM platform. The employed control core was TI's TMS320DSPF28335 microcontroller. Driving the system was an Asymmetric Half-Bridge Power Converter (AHBC). The torque measurement utilized a dedicated torque sensor, while the motor's actual speed was monitored using a high-resolution 15 bit Britt absolute encoder. Data exchange among components was facilitated through a CAN bus, illustrated in Figure 18.

Due to the experimental test precision and test environment, the simulation experiment results have errors with the results of physical verification, but it does not affect the verification of the results. The conventional DITC strategy and the control strategy proposed in this paper are used to compare and verify the motor, given a speed of 500 rpm and a load of 5 N·m, and the experimental results are shown in Figure 19 and 20. K_T is 22.1% under the conventional DITC control. Under the proposed control strategy in this paper, the hysteresis loop control strategy is designed for each of the two commutated subregions, which makes the torque transition in the TpE smoother, and the K_T is 14%.

To further verify the reliability of the proposed strategy, the load is raised to 10 N·m, and the rotational speed is maintained at 500 rpm. The waveforms are shown in Figures 21 and 22. Compared with the load of 5 N·m, the K_T of the proposed control strategy is further suppressed, and the K_T under the two control strategies are 25.1% and 11.39%, respectively.

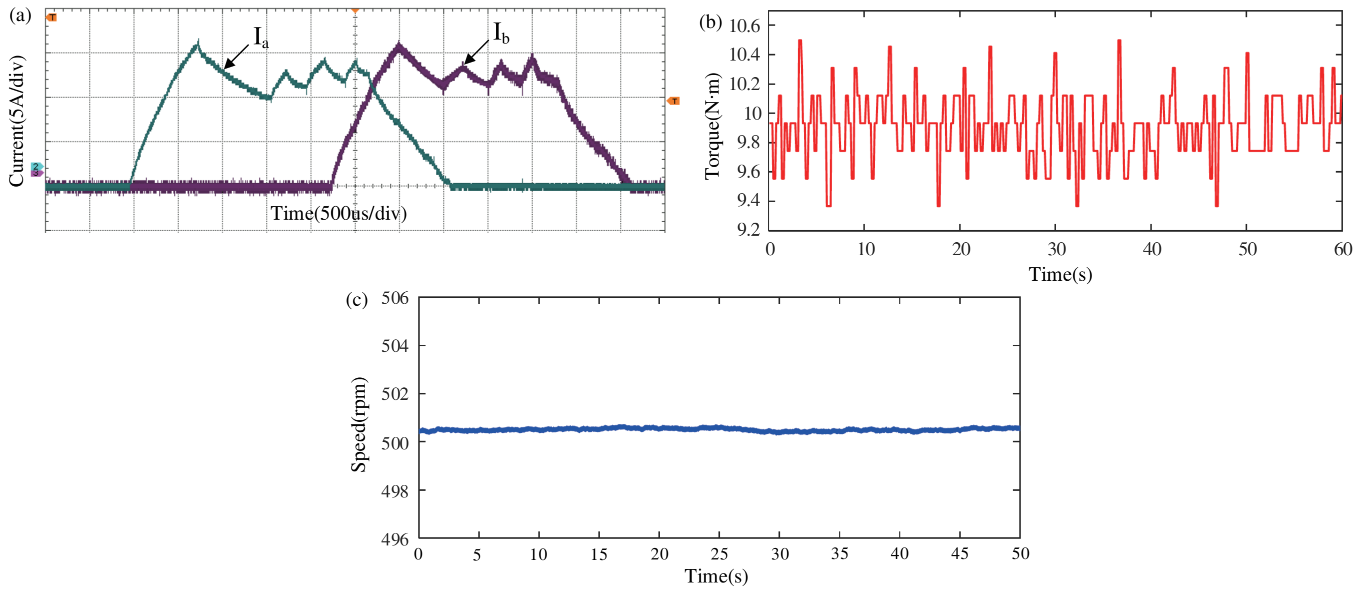

FIGURE 22. Current torque and speed waveforms under speed 500 rpm and load 10 N·m. (a) Current waveforms under the proposed strategy. (b) Torque waveforms under the proposed strategy. (c) Speed waveforms under the proposed strategy.

TABLE 2. Torque ripple comparison under two strategies.

Motor speed (rpm)	Load(N·m)	Torque ripple	
		K_{T1}	K_{T2}
500	5	15.6%	9.6%
500	10	16%	6.5%
1000	5	27%	9.4%
1000	10	×	7.5%

6. CONCLUSION

In this paper, we propose a current sensorless method to suppress interval torque ripple, thereby enhancing system reliability and reducing costs by eliminating the need for a current sensor. Leveraging motor position data, we derive motor acceleration through the second-order derivative of position with respect to time. This acceleration serves as feedback to demonstrate the equivalence between torque and acceleration control. It replaces the traditional torque loop and integrates into a dual closed-loop system with the speed loop for motor control. We thoroughly analyze the method's feasibility. Additionally, to mitigate torque ripple in the TpE region of the PMa-SRM, we analyze motor inductance characteristics and segment the TpE region into two subregions. We then develop an acceleration hysteresis loop control strategy for these regions to timely track reference acceleration. This approach facilitates the activation and deactivation of AHBC, reducing torque ripple during motor operation and ensuring stable torque output.

ACKNOWLEDGEMENT

This work was provided by National Natural Science Foundation of China (Grant No. 52167005) and Jiangxi Provincial Natural Science Foundation (Grant No. 20232BAB20406).

REFERENCES

[1] Sundaramoorthy, P., V. Arun, B. H. Kumar, J. Kavali, and M. Balaji, "Investigations on novel hybrid reluctance motor for electric vehicle applications," *IEEE Canadian Journal of Electrical and Computer Engineering*, Vol. 45, No. 4, 454–465, 2022.
[2] Sun, Q., J. Wu, and C. Gan, "Optimized direct instantaneous torque control for SRMs with efficiency improvement," *IEEE Transactions on Industrial Electronics*, Vol. 68, No. 3, 2072–2082, 2021.
[3] Bostanci, E., M. Moallem, A. Parsapour, and B. Fahimi, "Opportunities and challenges of switched reluctance motor drives for electric propulsion: A comparative study," *IEEE Transactions on Transportation Electrification*, Vol. 3, No. 1, 58–75, 2017.
[4] Li, S., S. Zhang, T. G. Habetler, and R. G. Harley, "Modeling, design optimization, and applications of switched reluctance machines — A review," *IEEE Transactions on Industry Applications*, Vol. 55, No. 3, 2660–2681, 2019.
[5] Han, G., H. Chen, and G. Guan, "Low-cost SRM drive system with reduced current sensors and position sensors," *IET Electric Power Applications*, Vol. 13, No. 7, 853–862, 2019.
[6] Ding, W., K. Li, and H. Fu, "Analysis of a 12/10-pole modular-stator hybrid-excited switched reluctance machine," *Transactions of China Electrotechnical Society*, Vol. 37, No. 8, 1948–1958, 2022.
[7] Diao, K., X. Sun, G. Lei, Y. Guo, and J. Zhu, "Multiobjective system level optimization method for switched reluctance motor drive systems using finite-element model," *IEEE Transactions on Industrial Electronics*, Vol. 67, No. 12, 10 055–10 064, 2020.
[8] Huang, C., H. Yuan, W. Cao, and Y. Wu, "Multi-objective optimization design of ERSRM with asymmetric stator poles," *Progress In Electromagnetics Research C*, Vol. 129, 257–271, 2023.
[9] Ma, M., K. Yuan, Q. Yang, S. Yang, and X. Zhang, "Segmented PWM variable duty ratio control of switched reluctance motor based on current soft chopper," *Proceedings of the CSEE*, Vol. 38, No. 18, 5582–5589, 2018.
[10] Xia, Z., G. Fang, D. Xiao, A. Emadi, and B. Bilgin, "An online torque sharing function method involving current dynamics for

switched reluctance motor drives," *IEEE Transactions on Transportation Electrification*, Vol. 9, No. 1, 534–548, 2023.

[11] Hu, Y., C. Gu, Z. Zhang, Z. Kang, and Y. Li, "Torque ripple minimization of six-phase switched reluctance motor based on enhanced direct instantaneous torque control," *IEEE Transactions on Transportation Electrification*, Vol. 10, No. 2, 4371–4382, 2024.

[12] Gou, L., C. Wang, M. Zhou, and X. You, "Integral sliding mode control for starting speed sensorless controlled induction motor in the rotating condition," *IEEE Transactions on Power Electronics*, Vol. 35, No. 4, 4105–4116, 2020.

[13] Verrelli, C. M., S. Bifaretti, E. Carfagna, A. Lidozzi, L. Solero, F. Crescimbini, and M. D. Benedetto, "Speed sensor fault tolerant PMSM machines: From position-sensorless to sensorless control," *IEEE Transactions on Industry Applications*, Vol. 55, No. 4, 3946–3954, 2019.

[14] Ha, J.-I., "Voltage injection method for three-phase current reconstruction in PWM inverters using a single sensor," *IEEE Transactions on Power Electronics*, Vol. 24, No. 3, 767–775, 2009.

[15] Sun, Q., J. Wu, C. Gan, Y. Hu, N. Jin, and J. Guo, "A new phase current reconstruction scheme for four-phase SRM drives using improved converter topology without voltage penalty," *IEEE Transactions on Industrial Electronics*, Vol. 65, No. 1, 133–144, 2017.

[16] Ye, H. and A. Emadi, "A six-phase current reconstruction scheme for dual traction inverters in hybrid electric vehicles with a single DC-link current sensor," *IEEE Transactions on Vehicular Technology*, Vol. 63, No. 7, 3085–3093, 2014.

[17] Cho, Y., T. LaBella, and J.-S. Lai, "A three-phase current reconstruction strategy with online current offset compensation using a single current sensor," *IEEE Transactions on Industrial Electronics*, Vol. 59, No. 7, 2924–2933, 2012.

[18] Jiang, W. and B. Fahimi, "Current reconstruction techniques for survivable three-phase PWM converters," *IEEE Transactions on Power Electronics*, Vol. 25, No. 1, 188–192, 2010.

[19] Youssef, A. B., S. K. E. Khil, and I. Slama-Belkhodja, "State observer-based sensor fault detection and isolation, and fault tolerant control of a single-phase PWM rectifier for electric railway traction," *IEEE Transactions on Power Electronics*, Vol. 28, No. 12, 5842–5853, 2013.

[20] Hafez, B., A. S. Abdel-Khalik, A. M. Massoud, S. Ahmed, and R. D. Lorenz, "Single-sensor-based three-phase permanent-magnet synchronous motor drive system with luenberger observers for motor line current reconstruction," *IEEE Transactions on Industry Applications*, Vol. 50, No. 4, 2602–2613, 2014.

[21] Salehifar, M., R. S. Arashloo, M. Moreno-Eguilaz, V. Sala, and L. Romeral, "Observer-based open transistor fault diagnosis and fault-tolerant control of five-phase permanent magnet motor drive for application in electric vehicles," *IET Power Electronics*, Vol. 8, No. 1, 76–87, 2015.

[22] Li, M., X. Chen, X. Ren, and Y. Li, "Position sensorless control strategy for switched reluctance motor based on typical position inductance," *Proceedings of the CSEE*, Vol. 37, No. 13, 3901–3908, 2017.